ACS MATERIALS LETTERS

www.acsmaterialsletters.org

LETTER

Nanotomography Investigation of 3D Printed Batteries with a Water-in-Salt Gel Polymer Electrolyte

Dean Yen, Cheng-Hung Lin, David J. Sprouster, Xiaoying Zheng, Xianghui Xiao, Wah-Keat Lee, Mingyuan Ge, and Yu-chen Karen Chen-Wiegart*

Cite This: *ACS Materials Lett.* 2023, 5, 1466–1475

Read Online

ACCESS | Metrics & More | Article Recommendations | Supporting Information

ABSTRACT: 3D printing, also known as additive manufacturing, has emerged as a promising strategy to design and fabricate future energy storage devices. Although significant progress has been reported, current 3D printed battery designs are still limited by the choice of the electrolyte, such as ceramic or conventional toxic organic electrolytes. Here, we incorporated the latest developments in aqueous batteries into a novel 3D printable battery that can be fabricated directly in an ambient environment that is also more environmentally friendly. Specifically, a gel polymer electrolyte with a water-in-salt concept was introduced in our 3D-printed batteries. Combining their advantages, the resulting 3D printable batteries show promise for much simplified processing conditions. The structural, (electro-)chemical, and morphological evolution batteries are being investigated by synchrotron X-ray nanotomography and electrochemical analysis. Overall, our research explores the possibility of an easier and more environmentally friendly way to build 3D printable, customizable batteries for future technologies.

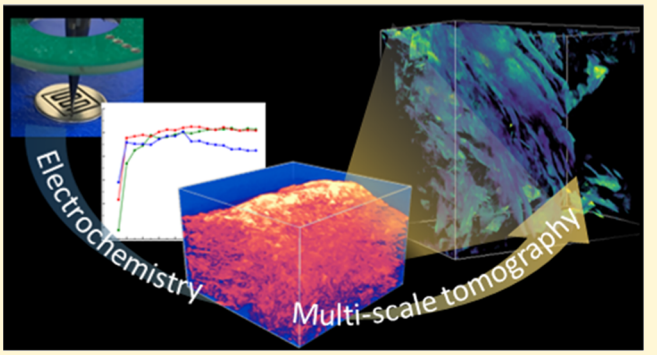

Additive manufacturing, also known as three-dimensional (3D) printing, emerged as a novel strategy to design electrochemical storage devices.[1] 3D printing provides the freedom of manufacturing batteries in arbitrary shapes and geometries, enabling applications such as wearable electronics and customizable batteries that can fit in desired applications, such as smart bracelets and bendable electronics.[2,3] In addition to the design freedom, 3D printing techniques provide a convenient way to accurately control the architecture of the electrode, providing opportunities to improve the ionic diffusion pathway and the wettability of the electrolyte. Such controllability results in better performance, such as a higher energy density, when compared with conventional planar designs.[4−9] Among various 3D printing methods, direct ink writing (DIW) is one of the most versatile methods for manufacturing energy storage devices. The DIW method utilizes simple extrusion-based technology without the need of highly specialized equipment and thus is very cost-effective.[10,11] Additionally, printable ink in DIW requires only a shear-thinning behavior. DIW thus provides a broad choice for 3D printing materials, including polymers, ceramic colloidal materials, and even metallic inks.[12,13]

Although the field of additive manufacturing is maturing, some fundamental challenges persist, which hamper the development of 3D printed batteries and their wide commercial use. For example, most printed batteries require the injection of a liquid electrolyte after printing the electrodes and packaging with enclosure or casings,[2,3,14] increasing the complexity of the manufacturing process. Flammable and toxic organic electrolytes lead to the need of incorporating airtight sealing and packaging of the devices into the manufacturing procedures.[15] In order to further reduce the cost and manufacturing of 3D printed batteries, designing a 3D printable electrode and electrolyte as well as their printing process that are compatible with an ambient atmosphere is critical. One possible solution is to employ an aqueous electrolyte instead of an organic electrolyte.

Received: December 1, 2022
Accepted: March 29, 2023
Published: April 11, 2023

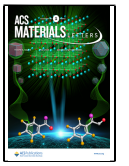

https://doi.org/10.1021/acsmaterialslett.2c01133
ACS Materials Lett. 2023, 5, 1466–1475

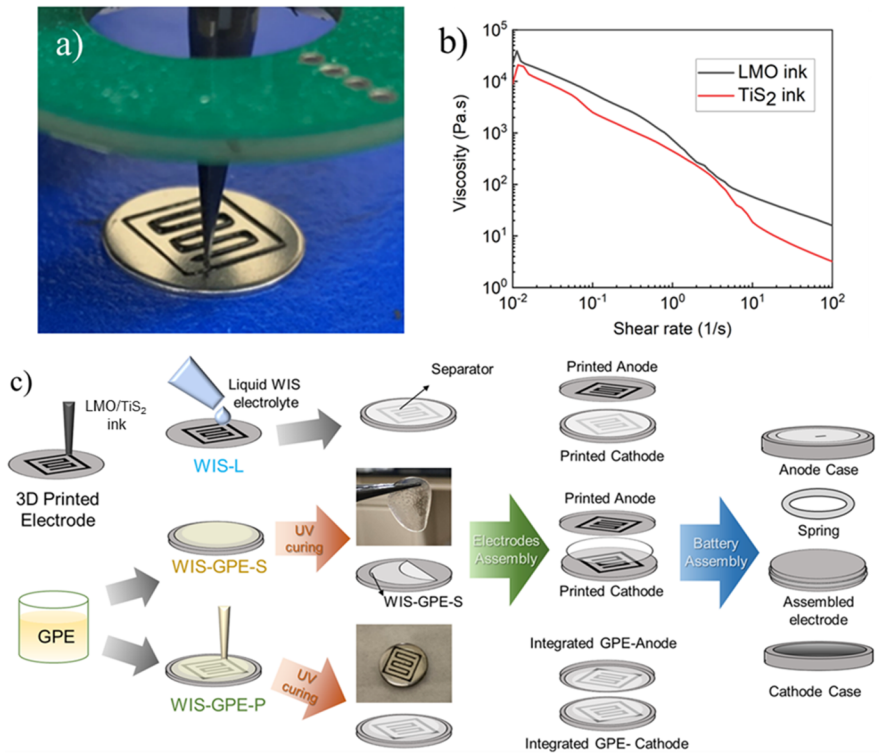

Figure 1. Preparation process of the WIS-GPE cell investigated in this work. (a) Printing of the LMO cathode electrode. (b) The rheology results of the prepared cathode and anode inks. (c) Schematic illustrating the three different configurations of printed batteries and their corresponding preparation routes.

Compared to organic electrolytes, aqueous electrolytes effectively reduce manufacturing difficulties as they possess improved compatibility with both water and air and therefore lower safety hazard risks. Although aqueous electrolytes possess a narrower operational voltage window when compared with their organic counterpart, various reports have shown that architectural engineering on the electrode and current collector through 3D printing can enhance the performance and provide competitive results.[16−19] On the other hand, water-in-salt (WIS) electrolytes developed recently have attracted interest. This interest is primarily because WIS electrolytes enable higher operation voltages and improved performance.[20] A novel strategy to reduce the cost and manufacturing of 3D printed batteries is to incorporate solid electrolytes into the 3D printing. Prior attempts to utilize solid electrolytes in 3D printed batteries have focused on ceramic electrolytes, which can only be printed at elevated temperatures. Moreover, although certain ceramic electrolytes possess high ionic conductivity (even at room temperature), they suffer from interface contact issues and often require high pressure to function.[21] Therefore, 3D printed batteries using a ceramic-based solid-state electrolyte are limited both in terms of their manufacturing requirements and end-use applications.[22,23]

A gel polymer electrolyte (GPE), a new type of electrolyte, has attracted attention in the field of battery research. GPEs usually consist of a polymer matrix, lithium salts, and a photo initializer. Using a UV light to cross-link the polymer network, a high ionic conductivity can be created. Such networks serve a dual functionality, both as the electrolyte and as the separator for the battery, simultaneously. Based on the polymer and salt selected, the property of the GPE can be tuned to exhibit good mechanical strength, flexibility, and high thermal stability.[24] The advantages of a WIS electrolyte can also be carried to the GPE, forming a Water-in-Salt-Gel Polymer Electrolyte (WIS-GPE) to combine the advantages of the two.[24,25] This combination of materials and printing strategies is ideal to easily manufacture 3D printable batteries that are inherently safe and can operate in air.

3D printing is a sophisticated engineering process where many engineering parameters can alter the physical and chemical states of the materials during printing, ultimately impacting the behavior of the printed structure. The electrode and electrolyte materials during the printing process are driven to far from equilibrium states, evolving into different structures and morphologies depending on the intrinsic materials properties and external stimuli.[26,27] Further understanding of the 3D morphology of printed battery electrodes and their corresponding electrochemistry is therefore required to design a 3D printable battery with desired properties.

Synchrotron X-ray methods have been widely applied to study batteries with conventional geometries, providing critical insights into the fundamental and practical understanding of battery operation and design.[28−31] There are, however, limited reports with such techniques in the field of 3D printed energy storage devices.[32] In the present work, we apply electrochemical analysis on printed $LiMn_2O_4$ (LMO) and TiS_2 electrodes cycled in different electrolytes, including a WIS electrolyte and a WIS-GPE, to investigate their performance and feasibility in various configurations. The printed structures were analyzed utilizing a combination of X-ray nanotomography and X-ray microtomography to correlate their electrochemical performance with a microstructure across multiple length scales.

Figure 1a demonstrates the printing of a battery electrode via DIW. The preparation process of the 3D-printable inks for the active materials were adapted from the workflow established in our previous work.[33] The electrode powders were prepared by

https://doi.org/10.1021/acsmaterialslett.2c01133
ACS Materials Lett. 2023, 5, 1466−1475

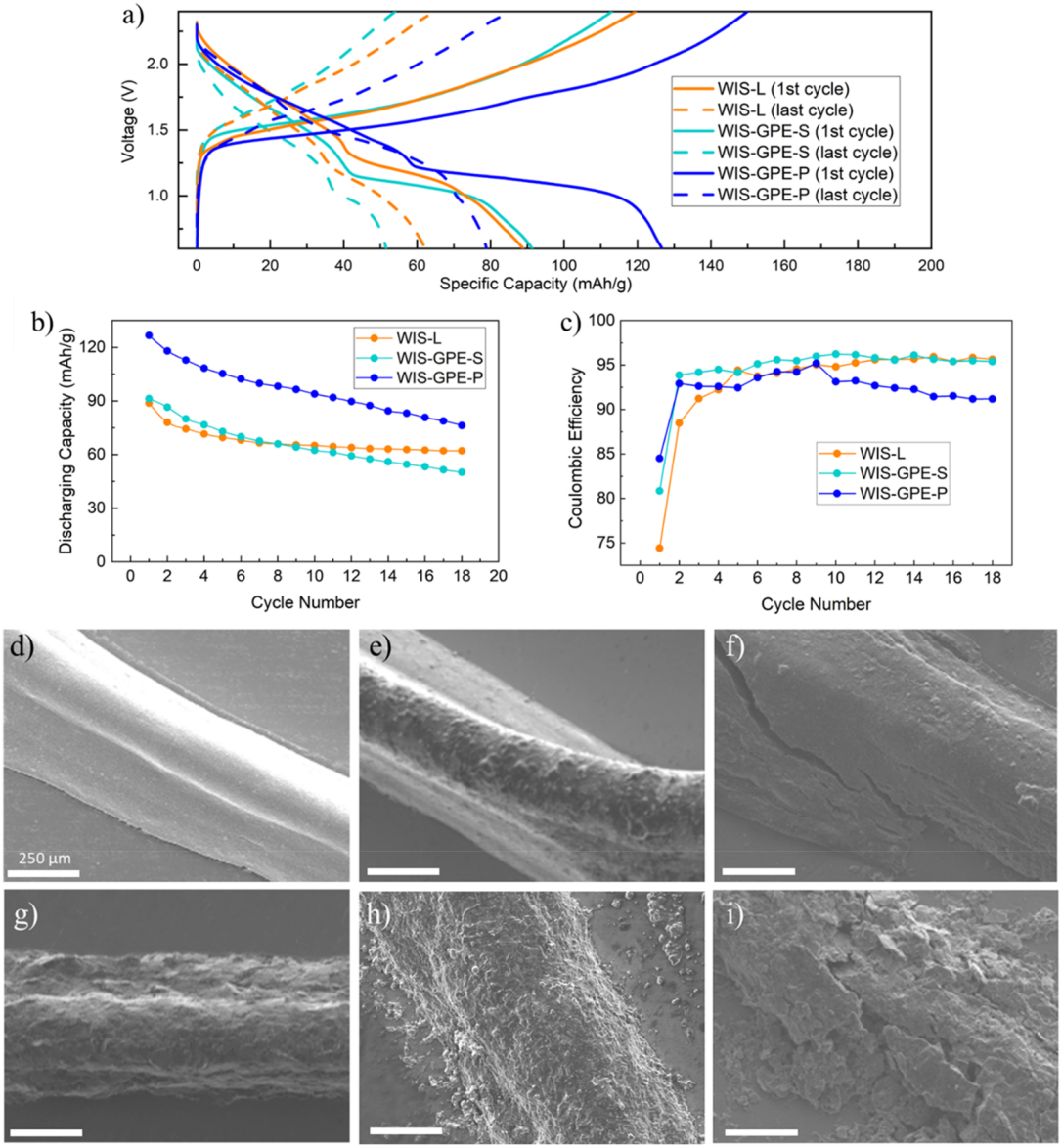

Figure 2. Electrochemical behavior of the cells with printed electrodes: (a) the cycling profile, (b) the discharging capacity profile, and (c) the Coulombic efficiency as a function of the cycles. SEM images of the pristine and printed electrodes: (d) the pristine LMO electrode, (e) the LMO electrode cycled in the WIS-GPE-S, and (f) the LMO electrode cycled in the WIS-L; (g) the pristine TiS_2 electrode, (h) the TiS_2 electrode cycled in the WIS-GPE-S, and (i) the TiS_2 electrode cycled in the WIS-L.

mixing active materials, conductive additive, and binder. Sodium carboxymethyl cellulose (SCC) was used instead of polyvinylidene fluoride (PVDF) as the rheological tuning agent, as it provides a stronger mechanical strength and a shear thinning property for the printable inks. Figure 1b shows the rheological data for both the LMO and TiS_2 inks. For both ink compositions, the viscosity decreases as the shear rate increases, indicating a shear-thinning behavior desired for the 3D printing process. The prepared powder was then dispersed within a mixture of water and ethylene glycol to form the ink. The cathode and anode were printed separately on two spacers for assembly. Three different types of cell configurations were constructed, as illustrated in Figure 1c. The first type is a WIS electrolyte in a liquid state, denoted as WIS-L. The WIS-L was used as a control sample to compare the two other samples with a solid-state gel polymer electrolyte. The solid-state gel polymer electrolyte as a separator, denoted as WIS-GPE-S, is the second generation investigated here. The WIS-GPE-S was developed to investigate the effects of using the gel polymer electrolyte on the electrochemical performance and the morphological evolution of the electrode. Finally, the gel polymer electrolyte was also printed directly on the printed electrode and then cured by a UV light source in place during the printing. This enabled the effective integration with the printed electrode structure. This third configuration is labeled as WIS-GPE-P and represents an integrated, 3D printable electrolyte-electrode component in a fully printed battery.

Figure 2a-c shows the electrochemical behaviors of the printed batteries with three types of configurations, including the charging and discharging curves for the first and last (18th) cycles (Figure 2a), the discharging capacity (Figure 2b), and Coulombic efficiency (CE) (Figure 2c) as a function of the cycle. For the cell configurations using GPEs, the electrochemical behavior is similar between the two configurations

https://doi.org/10.1021/acsmaterialslett.2c01133
ACS Materials Lett. 2023, 5, 1466−1475

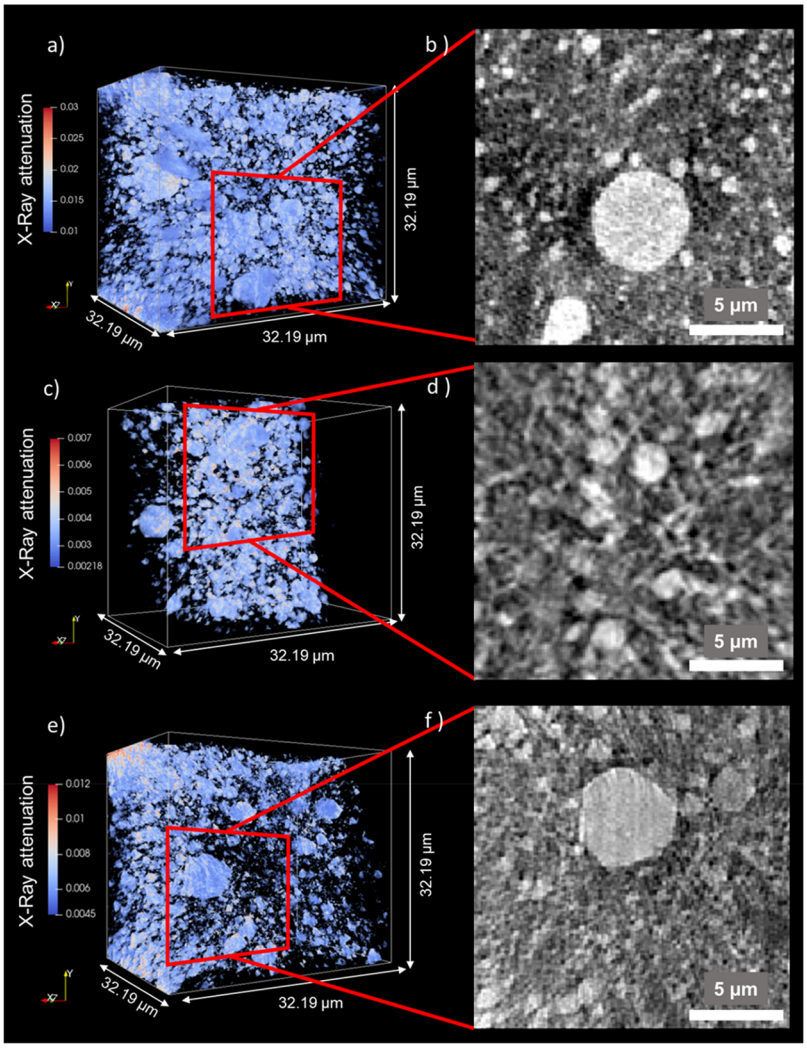

Figure 3. 3D X-ray nanotomography analysis showing the 3D volume rendering of the printed LMO electrodes (a, c, e) and their corresponding pseudocross-sectional images (b, d, f): (a,b) the pristine LMO electrode; (c,d) the LMO electrode cycled in the liquid WIS electrolyte, and (e,f) the LMO electrode cycled in the WIS-GPE-S.

(WIS-GPE-S and WIS-GPE-P). In the cycling profile, a plateau can be observed starting at 1.2 V and ending at 1 V for both of the GPE cells. This is potentially an indication of the transition between Li intercalation and the conversion reaction mechanisms, as reported in the literature for TiS_2[34−36] (Figure 2c), which occurs at a slightly lower voltage compared with the WIS-L cell and may be caused by the polarization difference between different electrolytes.

This consistent electrochemical behavior between the GPE cells can also be observed in the discharging profile (Figure 2b), where the WIS-L cell possesses a slightly different behavior. The capacity fade in the WIS-L cell slowed down after the fifth cycle; as for the two WIS-GPE cells, the trend of capacity fade continued as the number of cycles increased. A larger capacity loss can be observed for all three configurations; however, after the first cycle, the Coulombic efficiency becomes more stable for all cells. The low Coulombic efficiency in the first cycle may be due to the formation of the sulfur-based passivation film or solid electrolyte interface (SEI) layer, which is common within WIS systems.[34,35,37]

Although the GPE cells possess similar electrochemical behaviors, the discharging capacity of the WIS-GPE-P cell, where the WIS-GPE was integrated with the printed electrode, is higher than the WIS-GPE-S cell (Figure 2a,b), where the WIS-GPE was used only as a separator. This is likely due to the fact that the WIS-GPE was fully integrated with the electrode in the WIS-GPE-P cell, providing better interfacial contact between the electrode and electrolyte and thus creating a better ionic conductive network. Therefore, a higher portion of the active materials within the electrode can participate in the electrochemical reactions thereby contributing to the capacity. Although the Coulombic efficiency of the WIS-GPE-P cell is slightly lower than that of the WIS-GPE-S cell, the integrated structure still enabled the cell to retain a higher discharging capacity after almost 20 cycles, indicating the feasibility of using the WIS-GPE as a printable electrolyte to build printed batteries. While the starting discharging capacities are higher for both cells using GPEs, both of the GPE cells suffer from a more rapid capacity fade during the cycling process. However, despite having a lower Coulombic efficiency, the cell using the WIS-GPE-P still exhibited a higher discharging capacity at the end of the experiment when compared with the WIS-L cell. Considering the advantages of the GPE (enhanced safety and ease of manufacturing), our results demonstrate that using the WIS-GPE can be a viable strategy in continuing to advance the design of next-generation 3D printed batteries.

https://doi.org/10.1021/acsmaterialslett.2c01133
ACS Materials Lett. 2023, 5, 1466−1475

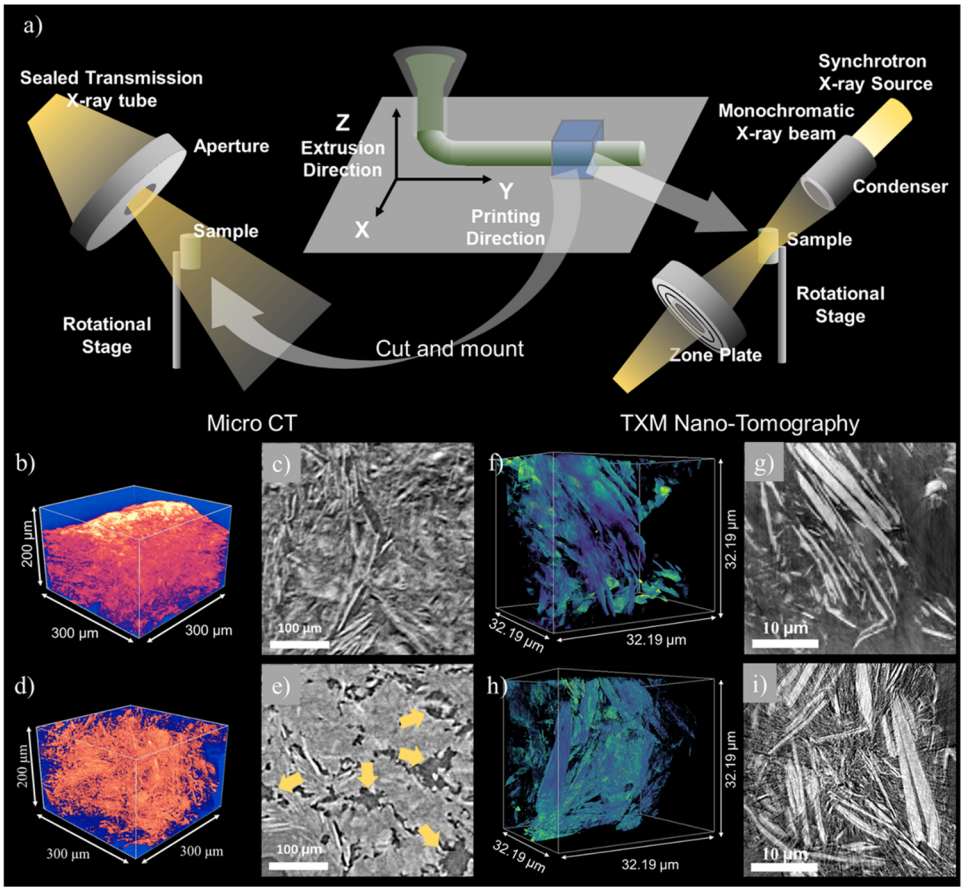

Figure 4. X-ray tomography study of the printed TiS_2 electrode. (a) A schematic showing how the printed geometry corresponds to the micro-CT sample; (b,c) micro-CT of the pristine TiS_2 electrode, (d,e) micro-CT of the TiS_2 electrode cycled in the WIS-GPE-S (Yellow arrows indicate the cracks formed by electrolyte aggregation.), (f,g) nanotomography of the pristine TiS_2 electrode, and (h,i) nanotomography of the TiS_2 electrode cycled in the WIS-GPE-S.

The SEM images of the pristine and cycled printed electrodes are shown in Figure 2d-h. The most notable difference between the cell using the liquid WIS electrolyte (WIS-L) and the cell using the WIS-GPE-P is the overall shape of the electrodes. Although both of the cells were assembled and cycled in a coin cell configuration and underwent a crimping process during the assembly, the morphology is very different for both cells. Compared with the pristine electrode (Figure 2d,g), the electrodes from the cell cycled in the liquid WIS electrolyte (Figure 2f,i) were flattened and possess cracks on the surface. In contrast, the electrodes cycled in the WIS-GPE preserve the original shape (Figure 2e,h). In addition to the shape difference, no apparent cracks were formed on the LMO electrode cycled in the WIS-GPE. The SEM images indicate that the WIS-GPE can serve as a protective layer to preserve the shape and integrity of the printed electrodes. This is potentially a contributing factor of why the cell using the WIS-GPE has a higher starting capacity than the cell using the WIS-L. The preservation of the overall 3D structure allows a better utilization of the electrodes and retains the advantages of using a 3D printed battery. Furthermore, the SEM-energy-dispersive X-ray spectroscopy (EDS) mapping is presented in Figures S1 and S2. The images show that some polymer residues were left on the electrode and could not be removed by physical peeling, blocking the Mn and Ti EDS signals of the cathode and anode materials, respectively. This indicates that the polymer has been sturdily integrated into the electrodes. It also shows that it will be challenging to investigate the electrode structure by 2D scanning probe microscopy alone, thus highlighting the importance of applying tomography analysis to unravel the detailed morphological change of the samples. These results suggest that the WIS-GPE can act as an improved electrolyte for 3D printed batteries, removing the need to introduce complicated cell designs.

X-ray nanotomography was performed to obtain the 3D images of the internal microstructure for the printed electrodes to further analyze the internal 3D morphology of the printed electrodes beneath the surface layer. The pristine electrodes, electrodes cycled in the liquid WIS electrolyte, and electrodes cycled in the WIS-GPE-S were investigated. The morphology characterization was carried out with TXM at Full Field X-ray Imaging (FXI) Beamline[38] at National Synchrotron Light Source II. Figure 3 shows the 3D volume rendering of the reconstructed X-ray nanotomography for the LMO electrodes, Figure 3(a,c,e) shows the tomographic reconstruction of the LMO electrodes, and Figure 3(b,d,f) shows the cross-sectional images of the regions highlighted by rectangles in Figure 3(a,c,e), respectively.

When comparing the three sets of tomographic reconstruction for the LMO electrodes, the cycled electrodes in different electrolytes (liquid WIS vs. WIS-GPE-S) exhibit different morphologies. The surface of the particles cycled in the liquid WIS electrolyte was smoother (Figure 3c-d), similar to the LMO particles in the pristine state (Figure 3a-b). For the electrodes cycled in the WIS-GPE, a rougher surface on the particles and

https://doi.org/10.1021/acsmaterialslett.2c01133
ACS Materials Lett. 2023, 5, 1466−1475

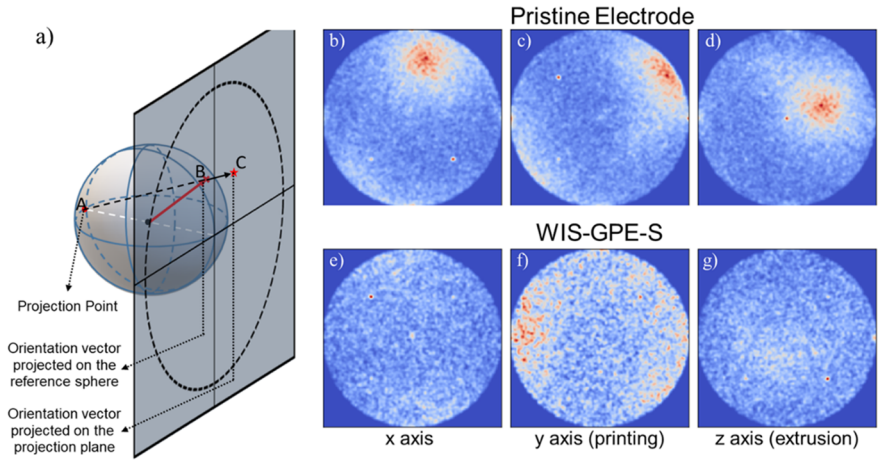

Figure 5. Interfacial Normal Distribution of the printed TiS_2 electrode along different axes: (a) concept of IND analysis, (b-d) the pristine electrode, and (e-g) the electrode cycled in the WIS-GPE-S.

scattered features, possibly indicating degraded electrolytes, were observed in the nanotomography reconstruction results (Figure 3e-f). Two sets of quantitative analyses were performed on the tomography to further analyze this observation. The results are summarized in Table S1 and Figure S5. The analysis based on the ImageJ plugin (Table S1) demonstrates the size difference between the three samples, showing that the pristine sample possesses the largest particle size. In contrast, the sample cycled in the WIS-L has the smallest particle size. Particle size analysis based on Euclidean distance transform reveals further details (Figure S5). The results show that the sample cycled in the WIS-L has the largest number of smaller particles and the least amount of particles larger than 1 μm in radius. Both results point to the conclusion that electrodes cycled in the WIS-L possesses smaller particle sizes. This observation suggests that particles cycled in the WIS-L underwent more dissolution during the cycling process, while the use of the WIS-GPE-S may have prevented the LMO particles from dissolving. While it is likely that the WIS-GPE-S can suppress LMO particle dissolution, as mentioned earlier, scattered features were observed in the WIS-GPE-S case, suggesting damage to the electrolyte. This damage is potentially reflective of the lower Coulombic efficiency (slightly > 90%) of the WIS-GPE-S compared to the CE of the WIS-L cell (>95%). The interaction between the GPE and electrode material involve many contributing factors, such as the choice of the plasticizer/solvent, lithium salt, or the base polymer, all of which can impact the behavior of the cell.[39,40] The degradation of the GPE can also occur during the reaction. In such a situation, electrode dissolution may occur when the cell contains a degraded GPE.[41]

TiS_2 particles possess plate-like morphologies and have the potential to align during printing and change during cycling. To investigate the microstructures pre- and postcycling, X-ray microcomputed tomography (micro-CT) was also performed on the printed TiS_2 electrode cycled in the WIS-GPE-S. The micro-CT and nanotomography combined provided a multi-scale 3D characterization of the system. Figure 4a illustrates the relationship between the printing geometry and tomography results. As shown in the prior section, for the LMO samples, no obvious difference was observed between pristine and cycled electrodes regarding particle and electrode morphology in the nanotomography. Comparing the TiS_2 samples, no major differences in particle shapes between pristine and cycled samples are apparent consistent with the nanotomography result. However, the macroscopic morphology of the electrode changes drastically after cycling in the WIS-GPE-S.

From the X-ray micro-CT, compared to the pristine sample (Figure 4b,c), the cycled sample (Figure 4d,e) showed that the electrolyte aggregates and fills pores in the electrode. A structure with more well-dispersed, small pores in the pristine electrode changed into one with larger gaps and cracks (as indicated by orange arrows) due to this electrolyte aggregation. The X-ray nanotomography reveals further details. In the pristine state (Figure 4f,g), the individual TiS_2 particles can be clearly identified. While in the cycled sample (Figure 4h,i), although the shape of the TiS_2 particles did not change, the surrounding structure has evolved. This is likely due to the WIS-GPE swelling and filling the electrode pores during the cycling process[42] or the degradation and volume change of the WIS-GPE, which then contributes to the morphological evolution. The formation of cracks could lead to the capacity loss, consistent with the lower Coulombic efficiency observed in both types of WIS-GPE cells, compared to the WIS-L cell.

In order to further investigate the differences in morphology between pristine and cycled samples, the morphological anisotropy of the printed electrodes was characterized by characterizing the Interfacial Normal Distribution (IND)[43,44] based on the tomographic reconstruction volumes. IND analysis characterizes the local surface orientation of the particles by calculating the surface normal from a mesh representing the surface of the particles. The surface normal was represented by a unit vector contained within a reference sphere, projected onto a plane via the stereographic projection method (Figure 5a). As shown in Figure 5b-d, the pristine and as-printed sample exhibits a slightly preferred morphological orientation along the x- and z-axes. This preferred orientation is close to the extrusion direction (z-axis). This is likely due to the alignment caused by the printing process and the substrate interaction as also observed in prior reports.[27,45,46] The shear force aligned the particles along the y-axis (printing) direction, and the surface normal of the plate-like TiS_2 particles then point toward the x- and z-axes due to this alignment. A stronger preferred orientation toward the z-axis (extrusion direction) was observed likely due to the plate-like morphology of the particles, which may stack up along the substrate.[47] On the other hand, the IND plots of the cycled electrode as shown in Figure 5c-g display a very different orientation distribution. Although a small extent of preferred orientation was still observed along the extrusion

https://doi.org/10.1021/acsmaterialslett.2c01133
ACS Materials Lett. 2023, 5, 1466−1475

direction, the cycled sample exhibits much less anisotropy when compared with its as-printed states. This may be due to the WIS-GPE swelling causing the deformation of the electrode and reducing the anisotropy of the TiS_2 particles' distribution as created by the printing process. As particle alignment can be a factor that determines the electrochemical behavior of the cells (such as ionic conductivity and impedance), the morphological and volume changes during the cycling should be considered when designing 3D printed batteries including the ones constructed with GPEs and other solid electrolytes.

In summary, we have designed and fabricated a form of less toxic ink for 3D printable batteries that can be prepared following simple procedures. Such electrode ink can be printed under ambient conditions by a simple extrusion-based direct-ink writing method. A WIS-GPE formula suitable for the LMO/TiS_2 system was also developed and applied to the printed electrodes. The electrochemical performance of the cell using the liquid WIS electrolyte and WIS-GPE was compared. The result shows that the cell using the WIS-L possesses a higher Coulombic efficiency, while the WIS-GPE has a higher starting discharging capacity and an overall higher retained capacity after 20 cycles. A combination of scanning electron microscopy, X-ray microtomography, and X-ray nanotomography was employed to characterize the surface and internal morphologies of the electrodes. The nanotomography revealed that although the WIS-GPE can help preserve the overall structure of the 3D printed electrode, compared to the cell using the liquid WIS electrolyte, the particles appear to degrade faster during the cycling process, resulting in the lower Coulombic for the cell using the WIS-GPE. Thus, further development of the printable ink and overall 3D printed battery architecture would be needed. 3D morphological analysis based on microtomography, coupled with nanotomography as a multiscale characterization, revealed the microstructure and particle alignment of the printed electrodes related to the printing process. Additionally, their morphological changes during the cycling, crack formation, and orientation redistribution of particles were also visualized and quantified using tomographic analysis. Our research shows that future work can be conducted to further understand the electrochemical behavior and morphological evolution of the electrodes. Overall, the WIS-GPE integrated printed electrodes possess a higher discharging capacity after cycling; combined with its relative ease of handling and integration with the 3D printing process and packaging, the WIS-GPE is a viable pathway toward building a fully 3D printable aqueous solid-state battery.

EXPERIMENTAL METHODS

Materials. $LiMn_2O_4$ (LMO, Sigma-Aldrich, USA), TiS_2 (Sigma-Aldrich, USA), sodium carboxymethyl cellulose (SCC, Sigma-Aldrich, USA), carbon black (Timical Super C65, MTI Corporation), ethylene glycol (EG, Sigma-Aldrich, USA), poly(ethylene glycol) methyl ether acrylate (MPEGA, average molar size = 480, Sigma-Aldrich, USA), 2-hydroxyethyl acrylate (HEA, Sigma-Aldrich, USA), poly(ethylene glycol) diacrylate (PEGDA, average molar size = 700, Sigma-Aldrich, USA), 2,2-dimethoxy-2-phenylacetophenone (DMPA), lithium bis-(trifluoromethanesulfonyl)imide (LiTFSI, Tokyo Chemical Industry), and lithium bis(pentafluoroethanesulfonyl)imide (LiBETI, Tokyo Chemical Industry) were used. All materials were used as purchased unless stated otherwise.

Ink Preparation. The preparation process of the 3D-printable inks for the active materials was adapted from the workflow established in our previous work.[33] The electrode powders were prepared by mixing 80 wt % of active materials (LMO for cathodes and TiS_2 for anodes), 10 wt % of SCC, and 10 wt % of carbon black. Afterward, the mixture was ground and mixed within the solvent by a planetary centrifugal mixer (SR-500M, Thinky USA). The mixture consists of 27 vol % of EG, and 73 vol % of deionized water was used as the solvent. The solid loading of the ink was chosen to be at 40%. This number was chosen to optimize the printability of the ink; if a higher solid loading is used, while it may provide a higher mechanical strength, it also increases the chance of clogging during printing.

Electrode Preparation. The well-mixed cathode and anode inks were then printed by using an extrusion-based 3D printing setup (Engine HR, Hyrel 3D, USA) by exerting force to the syringe. The printing was carried out using a direct ink writing method, with a nozzle size of 200 μm (Precision tips 27GA, Nordon EFD, USA); the printing speed was set to be at 200 mm/s, and the printing was conducted at room temperature. A snake-like pattern was printed directly on a stainless-steel spacer for electrochemical characterization. The pattern consists of two parts: the five layer inner structure and seven layer outer structure. The additional layers in the outer structure provide a structural integral during the assembling process. The height of each layer is ~150 μm after drying.

Electrolyte Preparation. The polymer mixture was prepared by mixing 89 wt % MPEGA, 9 wt % HEA, and 2 wt % PEGDA. 5 wt % DMPA was added as the photo initiator.[24] The liquid WIS electrolyte was prepared by dissolving LiTFSI and LiBETI in water with 27.8 molality (m), with a molar ratio of LiTFSI:LiBETI = 7:3.[37] The solution was heated at 70 °C and stirred until fully dissolved. The polymer and salt were then mixed in a 1:3 weight ratio to create the WIS-GPE. Five wt % of PVDF was added to the mixture as the rheology tuning agent.

Electrochemical Measurement. To test the cell performance, printed electrodes were assembled into CR2032 coin cells. The prepared WIS-GPE solution was then prepared into two types of configurations for an electrochemical test: 1) It was cured as a separator (WIS-GPE-S); 2) It was directly added onto the printed structure (WIS-GPE-P). A cell using a regular WIS electrolyte in the liquid state (WIS-L) was also prepared to compare their electrochemical behaviors. For configuration of the WIS-GPE-S, the WIS-GPE separator was prepared by casting the WIS-GPE on a Kapton film (Accu-Glass Products, USA), with the casting gap of 500 μm, and then UV cured by a UV array (PCA-365, Hyrel 3D, USA) integrated with the 3D printer for 20 min. The cured WIS-GPE was then peeled from the Kapton film and punched into round disks to be used as separators. The cell was then assembled with the printed cathode and anode, which sandwiched the cured separator WIS-GPE. For the configuration of the WIS-GPE-P, the WIS-GPE solution was printed directly onto both of the printed cathode and anode structures to cover the entire structure and cured by the UV array while printing; the structure was then cured for an additional 20 min under UV light to completely fixate the structure. The cell was then assembled by crimping two electrodes printed on spacers within the coin cell without any additional separators. For the WIS-L cell using the WIS electrolyte in the liquid state, the cell was assembled by crimping the printed electrodes' spring and separator (Celgard 2325). The electrochemical characterization was carried out under a constant current mode using a Bio-Logic VMP3 potentiostat, at a 0.1C rate, normalized by the capacity of the

https://doi.org/10.1021/acsmaterialslett.2c01133
ACS Materials Lett. 2023, 5, 1466−1475

LMO theoretical capacity value of 140 mAh/g[48] and a voltage window between 0.6 and 2.4 V for 18 cycles.[49]

Morphological Analysis. The surface morphology and SEM-EDS analysis of the printed electrodes were imaged by a Scanning Electron Microscope (SEM, JEOL 7600F) at the Center for Functional Nanomaterials (CFN) at BNL. The rheology characterization was performed using the Discovery HR-3 rheometer (TA Instruments) at CFN, BNL, using a steel Peltier plate with the diameter equal to 20 mm and the cone equal to 1.969° at 25 °C. The viscosity data were measured as a function of the shear rate (0.01 to 100 s^{-1}) in a logarithmically flow sweep mode.

The 3D X-ray nanotomography data was carried out by TXM at Full Field X-ray Imaging (FXI) Beamline at NSLS-II, Brookhaven National Laboratory (BNL). The samples were prepared by cutting the printed electrodes with a razor blade and then mounting them onto sample mounting pins for imaging. The X-ray energy was chosen to be ∼8 keV as an optimum energy at the FXI beamline. The field of view used was 32 μm. The microscope provides an optical resolution of approximately 30 nm.[38] The images obtained were first segmented by thresholding in an image processing software, ImageJ (Fiji),[50] and then imported into another software package, Tomviz (v.1.9.0),[51] for 3D visualization.

Morphological quantification using two different approaches was conducted to quantify the particle sizes from the tomography data. First, the reconstruction images were cropped and then segmented into binary images by ImageJ based on thresholding. For the first method, the particle size was quantified using the ImageJ plugin "Object counter 3D". For the second method, a python program developed in-house was then used to calculate the particle size distribution. A central circular mask was then applied to crop the central volume of interest that was in the depth-of-focus of the microscope. Euclidean distance transform was performed to determine the size of each particle. In distance transform, the shortest distance between every pixel of the active material phase to the border was calculated. For each particle, the maximum value in the distance map is considered as the size of the particle. To determine the volume fraction at a given size r, the volumes of all the particles with a size ≤ r (Vr) and with a size ≤ r+1 (Vr+1) were calculated. The ratio of the difference between the two volumes (Vr+1 − Vr) and the total volume is the volume fraction of the particle at size r.

X-ray microcomputed tomography (micro-CT) analysis was carried out on pristine and cycled 3D printed electrode samples at Stony Brook University (ZEISS Xradia 520 Versa). The tomography samples were prepared by two methods depending on the cycling state. For the pristine sample, the images were taken by imaging the electrode as printed on the stainless-steel substrates. For the cycled samples, the electrodes were first peeled off from the substrate and then mounted on a wood pin for imaging.

The X-ray source was operated at 80.19 kV and 87.47 uA (7W). The isotropic voxel size was set to 1 μm, and a series of 3201 projections were collected over 360° with a 3−6 s image exposure time per step. The total collection time for pristine samples is 5.3 and 2.7 h for cycled samples. The tomographic reconstruction was performed using a filtered-back projection algorithm using the software integrated with the microscope. The final data reconstruction results in a volumetric image size of 1016 × 984 × 991 for the TiS_2 samples and 1016 × 988 × 992 for the LMO samples. The reconstructed images were visualized also using Tomviz.

Interfacial Normal Distribution (IND) analysis was performed by extracting the surface normal data of the tomography using ParaView (v 4.3.1). Further data processing and visualization were then done using a python script developed in-house.

■ ASSOCIATED CONTENT

Supporting Information

The Supporting Information is available free of charge at https://pubs.acs.org/doi/10.1021/acsmaterialslett.2c01133.

Video of the volume rendering of microtomography of pristine TiS_2 electrode (MP4)
Video of the volume rendering of nanotomography of pristine TiS_2 electrode (MP4)
Video of the volume rendering of microtomography of TiS_2 electrode cycled in WIS-GPE-S (MP4)
Video of the volume rendering of nanotomography of TiS_2 electrode cycled in WIS-GPE-S (MP4)
Additional material characterization (PDF)

■ AUTHOR INFORMATION

Corresponding Author

Yu-chen Karen Chen-Wiegart − *Department of Materials Science and Chemical Engineering, Stony Brook University, Stony Brook, New York 11794, United States; National Synchrotron Light Source II, Brookhaven National Laboratory, Upton, New York 11973, United States;* orcid.org/0000-0003-4445-2159; Email: Karen.Chen-Wiegart@stonybrook.edu

Authors

Dean Yen − *Department of Materials Science and Chemical Engineering, Stony Brook University, Stony Brook, New York 11794, United States*

Cheng-Hung Lin − *National Synchrotron Light Source II, Brookhaven National Laboratory, Upton, New York 11973, United States;* orcid.org/0000-0001-9254-9751

David J. Sprouster − *Department of Materials Science and Chemical Engineering, Stony Brook University, Stony Brook, New York 11794, United States;* orcid.org/0000-0002-2689-0721

Xiaoying Zheng − *Department of Materials Science and Chemical Engineering, Stony Brook University, Stony Brook, New York 11794, United States*

Xianghui Xiao − *National Synchrotron Light Source II, Brookhaven National Laboratory, Upton, New York 11973, United States*

Wah-Keat Lee − *National Synchrotron Light Source II, Brookhaven National Laboratory, Upton, New York 11973, United States*

Mingyuan Ge − *National Synchrotron Light Source II, Brookhaven National Laboratory, Upton, New York 11973, United States;* orcid.org/0000-0001-5682-7443

Complete contact information is available at: https://pubs.acs.org/10.1021/acsmaterialslett.2c01133

Author Contributions

CRediT: **Dean Yen** data curation, formal analysis, investigation, validation, visualization, writing-original draft; **Cheng-Hung Lin** data curation, investigation; **David Sprouster** data curation,

https://doi.org/10.1021/acsmaterialslett.2c01133
ACS Materials Lett. 2023, 5, 1466−1475

visualization; **Xiaoyin Zheng** formal analysis; **Xianghui Xiao** data curation, methodology; **Wah-Keat Lee** data curation, methodology; **Mingyuan Ge** data curation, visualization; **Yu-chen Karen Chen-Wiegart** conceptualization, data curation, funding acquisition, investigation, methodology, project administration, resources, software, supervision, validation, writing-review & editing.

Notes

The authors declare no competing financial interest.

■ ACKNOWLEDGMENTS

This work was supported by the Seed Funding Energy Systems for Sustainability Research, funded by the College of Engineering and Applied Sciences, Stony Brook University. This research used FXI beamline (18-ID) and resources of the National Synchrotron Light Source II, a U.S. Department of Energy (DOE) Office of Science User Facility operated for the DOE Office of Science by Brookhaven National Laboratory under Contract No. DE-SC0012704. This research used Materials Synthesis and Characterization Facility of the Center for Functional Nanomaterials (CFN), which is a U.S. DOE Office of Science Facility, at Brookhaven National Laboratory under Contract No. DE-SC0012704. This research used an XCT instrument. D.J. Sprouster acknowledges the U.S. DOE Office of Fusion Energy Sciences under Contract No. DE-SC0018322 with the Research Foundation for the State University of New York at Stony Brook.

■ REFERENCES

(1) Chang, P.; Mei, H.; Zhou, S. X.; Dassios, K. G.; Cheng, L. F. 3D printed electrochemical energy storage devices. *J. Mater. Chem. A* **2019**, *7*, 4230−4258.

(2) Chen, C. L.; Jiang, J. M.; He, W. J.; Lei, W.; Hao, Q. L.; Zhang, X. G. 3D Printed High-Loading Lithium-Sulfur Battery Toward Wearable Energy Storage. *Adv. Funct. Mater.* **2020**, *30*, 1909469.

(3) Praveen, S.; Santhoshkumar, P.; Joe, Y. C.; Senthil, C.; Lee, C. W. 3D-printed architecture of Li-ion batteries and its applications to smart wearable electronic devices. *Appl. Mater. Today* **2020**, *20*, 100688.

(4) Cakici, M.; Reddy, K. R.; Alonso-Marroquin, F. Advanced electrochemical energy storage supercapacitors based on the flexible carbon fiber fabric-coated with uniform coral-like MnO2 structured electrodes. *Chem. Eng. J.* **2017**, *309*, 151−158.

(5) Chen, K. F.; Xue, D. F. Materials chemistry toward electrochemical energy storage. *J. Mater. Chem. A* **2016**, *4*, 7522−7537.

(6) Fu, K.; Yao, Y. G.; Dai, J. Q.; Hu, L. B. Progress in 3D Printing of Carbon Materials for Energy-Related Applications. *Adv. Mater.* **2017**, *29*, 1603486.

(7) Gao, J.; Li, L.; Tan, J. W.; Sun, H.; Li, B. C.; Idrobo, J. C.; Singh, C. V.; Lu, T. M.; Koratkar, N. Vertically Oriented Arrays of ReS2 Nanosheets for Electrochemical Energy Storage and Electrocatalysis. *Nano Lett.* **2016**, *16*, 3780−3787.

(8) Izumi, A.; Sanada, M.; Furuichi, K.; Teraki, K.; Matsuda, T.; Hiramatsu, K.; Munakata, H.; Kanamura, K. Rapid charge and discharge property of high capacity lithium ion battery applying three-dimensionally patterned electrode. *J. Power Sources* **2014**, *256*, 244−249.

(9) Wang, J. G.; Liu, H. Z.; Sun, H. H.; Hua, W.; Wang, H. W.; Liu, X. R.; Wei, B. Q. One-pot synthesis of nitrogen-doped ordered mesoporous carbon spheres for high-rate and long-cycle life supercapacitors. *Carbon* **2018**, *127*, 85−92.

(10) Chen, P.-Y.; Liu, M.; Wang, Z.; Hurt, R. H.; Wong, I. Y. From Flatland to Spaceland: Higher Dimensional Patterning with Two-Dimensional Materials. *Adv. Mater.* **2017**, *29*, 1605096.

(11) Zhu, C.; Liu, T.; Qian, F.; Chen, W.; Chandrasekaran, S.; Yao, B.; Song, Y.; Duoss, E. B.; Kuntz, J. D.; Spadaccini, C. M.; Worsley, M. A.; Li, Y. 3D printed functional nanomaterials for electrochemical energy storage. *Nano Today* **2017**, *15*, 107−120.

(12) Lewis, J. A.; Smay, J. E.; Stuecker, J.; Cesarano, J., III Direct ink writing of three-dimensional ceramic structures. *J. Am. Ceram. Soc.* **2006**, *89*, 3599−3609.

(13) Skylar-Scott, M. A.; Gunasekaran, S.; Lewis, J. A. Laser-assisted direct ink writing of planar and 3D metal architectures. *Proc. Natl. Acad. Sci. U.S.A.* **2016**, *113*, 6137−6142.

(14) Wei, S.; Qu, G.; Luo, G.; Huang, Y.; Zhang, H.; Zhou, X.; Wang, L.; Liu, Z.; Kong, T. Scalable and Automated Fabrication of Conductive Tough-Hydrogel Microfibers with Ultrastretchability, 3D Printability, and Stress Sensitivity. *ACS Appl. Mater. Interfaces* **2018**, *10*, 11204−11212.

(15) Wei, M.; Zhang, F.; Wang, W.; Alexandridis, P.; Zhou, C.; Wu, G. 3D direct writing fabrication of electrodes for electrochemical storage devices. *J. Power Sources* **2017**, *354*, 134−147.

(16) Gao, W. L.; Pumera, M. 3D Printed Nanocarbon Frameworks for Li-Ion Battery Cathodes. *Adv. Funct. Mater.* **2021**, *31*, 2007285.

(17) Gao, W. L.; Michalicka, J.; Pumera, M. Hierarchical Atomic Layer Deposited V2O5 on 3D Printed Nanocarbon Electrodes for High-Performance Aqueous Zinc-Ion Batteries. *Small* **2022**, *18*, 2105572.

(18) Ji, D. F.; Zheng, H. Y.; Zhang, H.; Liu, W. Q.; Ding, J. W. 3D printed high-performance sodium ion and zinc ion full batteries. *J. Alloys Compd.* **2022**, *900*, 163394.

(19) Wu, B. K.; Guo, B. B.; Chen, Y. Z.; Mu, Y. B.; Qu, H. Q.; Lin, M.; Bai, J. M.; Zhao, T. S.; Zeng, L. High Zinc Utilization Aqueous Zinc Ion Batteries Enabled by 3D Printed Graphene Arrays. *Energy Storage Mater.* **2023**, *54*, 75−84.

(20) Lin, C. H.; Sun, K.; Ge, M. Y.; Housel, L. M.; McCarthy, A. H.; Vila, M. N.; Zhao, C. H.; Xiao, X. H.; Lee, W. K.; Takeuchi, K. J.; Takeuchi, E. S.; Marschilok, A. C.; Chen-Wiegart, Y. C. K. Systems-level investigation of aqueous batteries for understanding the benefit of water-in-salt electrolyte by synchrotron nanoimaging. *Sci. Adv.* **2020**, *6*, eaay7129.

(21) Zhao, Q.; Stalin, S.; Zhao, C. Z.; Archer, L. A. Designing solid-state electrolytes for safe, energy-dense batteries. *Nature Reviews Materials* **2020**, *5*, 229−252.

(22) Cheng, M.; Jiang, Y. Z.; Yao, W. T.; Yuan, Y. F.; Deivanayagam, R.; Foroozan, T.; Huang, Z. N.; Song, B.; Rojaee, R.; Shokuhfar, T.; Pan, Y. Y.; Lu, J.; Shahbazian-Yassar, R. Elevated-Temperature 3D Printing of Hybrid Solid-State Electrolyte for Li-Ion Batteries. *Adv. Mater.* **2018**, *30*, 1800615.

(23) Cheng, M.; Ramasubramanian, A.; Rasul, M. G.; Jiang, Y. Z.; Yuan, Y. F.; Foroozan, T.; Deivanayagam, R.; Saray, M. T.; Rojaee, R.; Song, B.; Yurkiv, V. R.; Pan, Y. Y.; Mashayek, F.; Shahbazian-Yassar, R. Direct Ink Writing of Polymer Composite Electrolytes with Enhanced Thermal Conductivities. *Adv. Funct. Mater.* **2021**, *31*, 2006683.

(24) Langevin, S. A.; Tan, B.; Freeman, A. W.; Gagnon, J. C.; Hoffman, C. M.; Logan, M. W.; Maranchi, J. P.; Gerasopoulos, K. UV-cured gel polymer electrolytes with improved stability for advanced aqueous Li-ion batteries. *Chem. Commun.* **2019**, *55*, 13085−13088.

(25) Logan, M. W.; Langevin, S.; Tan, B.; Freeman, A. W.; Hoffman, C.; Trigg, D. B.; Gerasopoulos, K. UV-cured eutectic gel polymer electrolytes for safe and robust Li-ion batteries. *J. Mater. Chem. A* **2020**, *8*, 8485−8495.

(26) Lin, C.-H.; Dyro, K.; Chen, O.; Yen, D.; Zheng, B.; Arango, M. T.; Bhatia, S.; Sun, K.; Meng, Q.; Wiegart, L.; Chen-Wiegart, Y.-c. K. Revealing meso-structure dynamics in additive manufacturing of energy storage via operando coherent X-ray scattering. *Appl. Mater. Today* **2021**, *24*, 101075.

(27) Torres Arango, M.; Zhang, Y.; Zhao, C.; Li, R.; Doerk, G.; Nykypanchuk, D.; Chen-Wiegart, Y. C. K.; Fluerasu, A.; Wiegart, L. Ink-substrate interactions during 3D printing revealed by time-resolved coherent X-ray scattering. *Materials Today Physics* **2020**, *14*, 100220.

(28) Gong, Z. L.; Yang, Y. The application of synchrotron X-ray techniques to the study of rechargeable batteries. *Journal of Energy Chemistry* **2018**, *27*, 1566−1583.

https://doi.org/10.1021/acsmaterialslett.2c01133
ACS Materials Lett. 2023, 5, 1466−1475

(29) Heenan, T. M. M.; Tan, C.; Hack, J.; Brett, D. J. L.; Shearing, P. R. Developments in X-ray tomography characterization for electrochemical devices. *Mater. Today* **2019**, *31*, 69−85.
(30) Cao, C. T.; Toney, M. F.; Sham, S. K.; Harder, R.; Shearing, P. R.; Xiao, X. H.; Wang, J. J. Emerging X-ray imaging technologies for energy materials. *Mater. Today* **2020**, *34*, 132−147.
(31) Ford, H. O.; Park, B.; Jiang, J. Z.; Seidler, M. E.; Schaefer, J. L. Enhanced Li+ Conduction within Single-Ion Conducting Polymer Gel Electrolytes via Reduced Cation-Polymer Interaction. *Acs Materials Letters* **2020**, *2*, 272−279.
(32) Jha, S.; Chen, Y.; Zhang, B.; Elwany, A.; Parkinson, D.; Liang, H. Influence of morphology on electrochemical and capacity performance of open-porous structured electrodes. *J. Appl. Electrochem.* **2020**, *50*, 231−244.
(33) Sun, K.; Wei, T.-S.; Ahn, B. Y.; Seo, J. Y.; Dillon, S. J.; Lewis, J. A. 3D Printing of Interdigitated Li-Ion Microbattery Architectures. *Adv. Mater.* **2013**, *25*, 4539−4543.
(34) Fu, M. S.; Yao, Z. P.; Ma, X.; Dong, H.; Sun, K.; Hwang, S.; Hu, E. Y.; Gan, H.; Yao, Y.; Stach, E. A.; Wolverton, C.; Su, D. Expanded lithiation of titanium disulfide: Reaction kinetics of multi-step conversion reaction. *Nano Energy* **2019**, *63*, 103882.
(35) Sun, W.; Suo, L. M.; Wang, F.; Eidson, N.; Yang, C. Y.; Han, F. D.; Ma, Z. H.; Gao, T.; Zhu, M.; Wang, C. S. "Water-in-Salt" electrolyte enabled LiMn2O4/TiS2 Lithium-ion batteries. *Electrochem. Commun.* **2017**, *82*, 71−74.
(36) Zhang, L.; Sun, D.; Kang, J.; Wang, H. T.; Hsieh, S. H.; Pong, W. F.; Bechtel, H. A.; Feng, J.; Wang, L. W.; Cairns, E. J.; Guo, J. H. Tracking the Chemical and Structural Evolution of the TiS2 Electrode in the Lithium-Ion Cell Using Operando X-ray Absorption Spectroscopy. *Nano Lett.* **2018**, *18*, 4506−4515.
(37) Yamada, Y.; Usui, K.; Sodeyama, K.; Ko, S.; Tateyama, Y.; Yamada, A. Hydrate-melt electrolytes for high-energy-density aqueous batteries. *Nature Energy* **2016**, *1*, 16129.
(38) Ge, M. Y.; Coburn, D. S.; Nazaretski, E.; Xu, W. H.; Gofron, K.; Xu, H. J.; Yin, Z. J.; Lee, W. K. One-minute nano-tomography using hard X-ray full-field transmission microscope. *Appl. Phys. Lett.* **2018**, *113*, 083109.
(39) Baskoro, F.; Wong, H. Q.; Yen, H. J. Strategic Structural Design of a Gel Polymer Electrolyte toward a High Efficiency Lithium-Ion Battery. *Acs Applied Energy Materials* **2019**, *2*, 3937−3971.
(40) Hassoun, J.; Scrosati, B. Review-Advances in Anode and Electrolyte Materials for the Progress of Lithium-Ion and beyond Lithium-Ion Batteries. *J. Electrochem. Soc.* **2015**, *162*, A2582−A2588.
(41) Dias, F. B.; Plomp, L.; Veldhuis, J. B. J. Trends in polymer electrolytes for secondary lithium batteries. *J. Power Sources* **2000**, *88*, 169−191.
(42) Yin, D. W.; de la Cruz, M. O.; de Pablo, J. J. Swelling and collapse of polyelectrolyte gels in equilibrium with monovalent and divalent electrolyte solutions. *J. Chem. Phys.* **2009**, *131*, 194907.
(43) Chen, Y. C. K.; Chu, Y. S.; Yi, J.; McNulty, I.; Shen, Q.; Voorhees, P. W.; Dunand, D. C. Morphological and topological analysis of coarsened nanoporous gold by x-ray nanotomography. *Appl. Phys. Lett.* **2010**, *96*, 043122.
(44) Kammer, D.; Voorhees, P. W. The morphological evolution of dendritic microstructures during coarsening. *Acta Mater.* **2006**, *54*, 1549−1558.
(45) Lewicki, J. P.; Rodriguez, J. N.; Zhu, C.; Worsley, M. A.; Wu, A. S.; Kanarska, Y.; Horn, J. D.; Duoss, E. B.; Ortega, J. M.; Elmer, W.; Hensleigh, R.; Fellini, R. A.; King, M. J. 3D-Printing of Meso-structurally Ordered Carbon Fiber/Polymer Composites with Unprecedented Orthotropic Physical Properties. *Sci. Rep.* **2017**, *7*, 43401.
(46) Hausmann, M. K.; Ruhs, P. A.; Siqueira, G.; Lauger, J.; Libanori, R.; Zimmermann, T.; Studart, A. R. Dynamics of Cellulose Nanocrystal Alignment during 3D Printing. *ACS Nano* **2018**, *12*, 6926−6937.
(47) Chen-Wiegart, Y. C. K.; Figueroa-Santos, M. A.; Petrash, S.; Garcia-Miralles, J.; Wang, J. Critical factors affecting the 3D microstructural formation in hybrid conductive adhesive materials studied by X-ray nano-tomography. *Nanoscale* **2015**, *7*, 908−913.
(48) Xia, H.; Luo, Z. T.; Xie, J. P. Nanostructured LiMn2O4 and their composites as high-performance cathodes for lithium-ion batteries. *Progress in Natural Science-Materials International* **2012**, *22*, 572−584.
(49) Sun, W.; Suo, L.; Wang, F.; Eidson, N.; Yang, C.; Han, F.; Ma, Z.; Gao, T.; Zhu, M.; Wang, C. Water-in-Salt" electrolyte enabled LiMn2O4/TiS2 Lithium-ion batteries. *Electrochem. Commun.* **2017**, *82*, 71−74.
(50) Schindelin, J.; Arganda-Carreras, I.; Frise, E.; Kaynig, V.; Longair, M.; Pietzsch, T.; Preibisch, S.; Rueden, C.; Saalfeld, S.; Schmid, B.; Tinevez, J. Y.; White, D. J.; Hartenstein, V.; Eliceiri, K.; Tomancak, P.; Cardona, A. Fiji: an open-source platform for biological-image analysis. *Nat. Methods* **2012**, *9*, 676−682.
(51) Tomviz.org. https://tomviz.org/ (accessed 2022-12-21).

https://doi.org/10.1021/acsmaterialslett.2c01133
ACS Materials Lett. 2023, 5, 1466−1475